MRI-Inspired High-Resolution Localization for Biomedical Applications

Azita Emami and Manuel Monge

Artificial nuclear spins on a chip

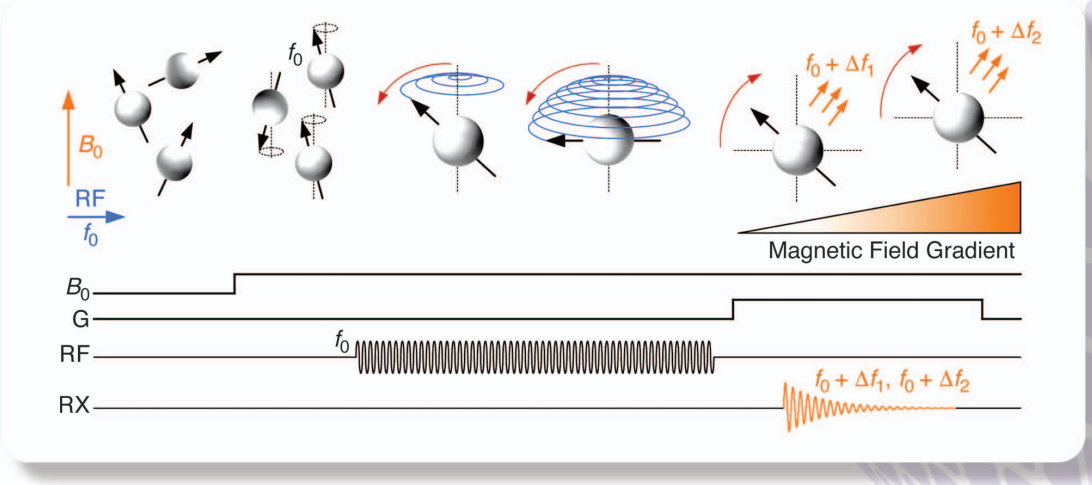

FOOTAGE FIRM, INC.

Significant advances have been made recently toward technologies such as smart pills to image the gastrointestinal tract [1], distributed sensors to map the function of the brain [2], and microscale swimming robots to access organs through the bloodstream [3]. Such technologies promise new ways to diagnose and treat diseases of local pathology, including neurodegeneration, autoimmune disease, cancer, and atherosclerosis. In fact, wireless microscale devices that navigate the body to diagnose and treat disease are key elements of the future of medicine, addressing localized malfunction in neurological,

Digital Object Identifier 10.1109/MSSC.2018.2867406
Date of publication: 16 November 2018

1943-0582/18©2018IEEE

cardiovascular, autoimmune, cancer, and other disease areas.

Although substantial progress has been made in endowing microscale devices with capabilities for sensing their environment, releasing drugs, and even propelling themselves through the body [4], a major challenge remains in localizing, controlling, and communicating with these devices. Currently, there are no effective means to precisely determine the location of microscale devices deep inside the body and communicate with them in a location-specific manner. Existing methods based on near-field electromagnetic interactions fail to provide accurate, unambiguous localization and typically cannot interface with multiple devices at once [4], [5]. Methods based on ionizing radiation (e.g., X-rays) pose safety risks and can only visualize, and not transmit, information to specific devices. For the vision of smart wireless devices navigating the body to diagnose and treat disease to come to full fruition, a breakthrough is needed in microscale device localization.

To address this need, we take inspiration from another biomedical technology: magnetic resonance imaging (MRI). MRI measures signals from nuclear spins, each of which acts as an atom-sized transmitter resonating at a magnetic field-dependent frequency. MRI can distinguish the locations of more than 10^{26} spins in the body with ~100-μm precision by encoding the location of nuclei in the frequency at which they absorb and emit signals. A magnetic field gradient is applied such that nuclei in one location resonate at a predictably different frequency from nuclei at another location. These frequency shifts are then used to map the observed signals

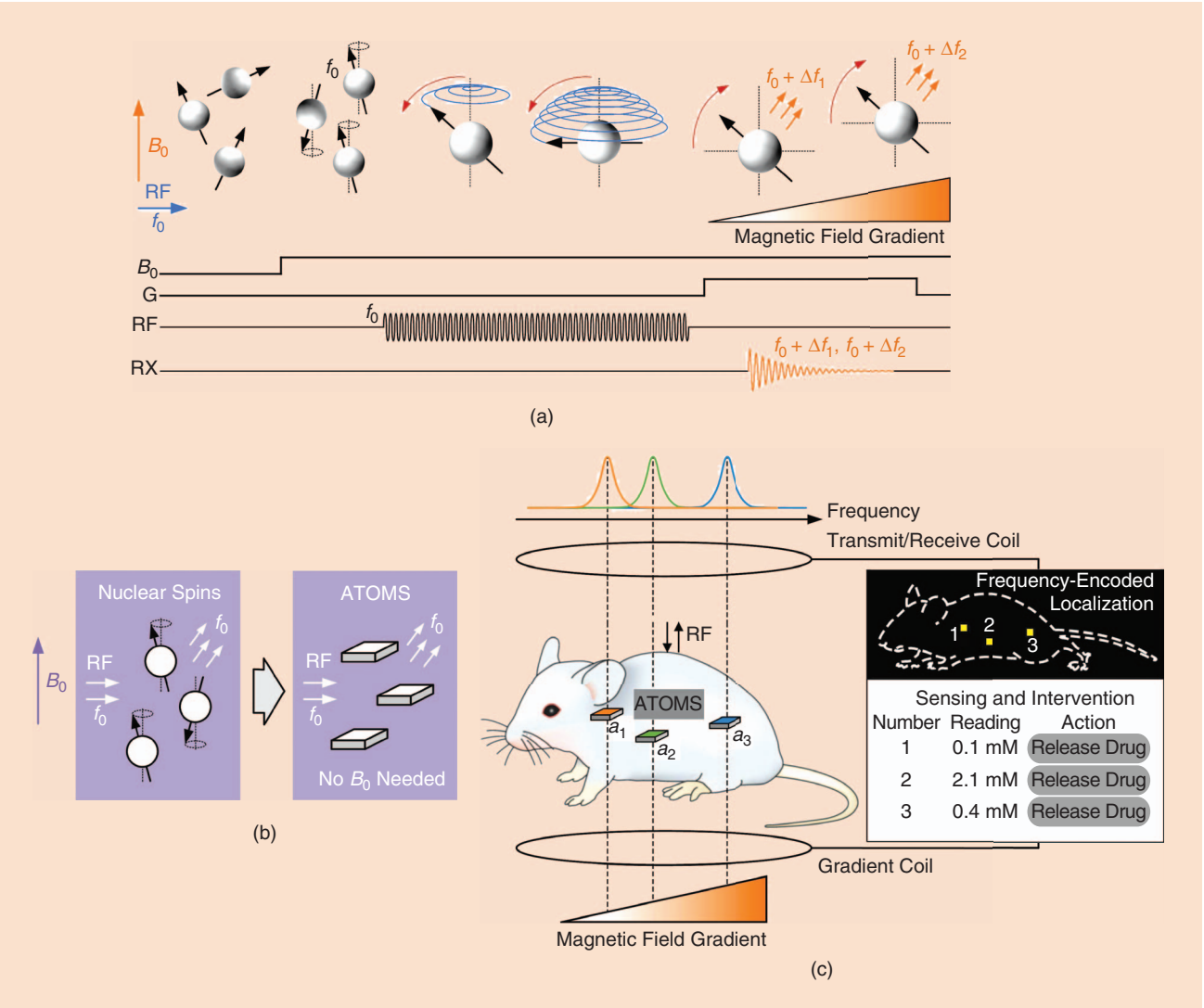

FIGURE 1: (a) The operating principle of MRI. When a polarizing magnetic field (B_0) is applied, randomly oriented nuclear spins align to B_0 and start precessing at a known frequency f_0 (Larmor frequency). Then, after excitation by an RF signal at f_0, the nuclear spins radiate back a signal at a frequency that is shifted relative to f_0 proportional to an applied magnetic field gradient. Thus, their location can be determined by mapping the received signals in space. (b) ATOMS mimic the behavior of nuclear spins in an MRI. It is important to note that B_0 (the magnetic field generated by the superconductive MRI magnet) is not required. (c) ATOMS are microscale devices capable of power harvesting and communication at magnetic field-dependent frequencies. When multiple ATOMS are in an animal or patient, their locations are discerned by applying a magnetic field gradient. (Figure taken from [6].)

in space [Figure 1(a)]. Conversely, one can excite nuclei selectively by applying field gradients during frequency-specific transmission.

In this work [6], we propose to adapt the principle of spatial frequency encoding to localize and communicate with distributed electronic microsensors in vivo. Specifically, we have developed a new class of microscale circuits that operates at magnetic field-dependent frequencies, enabling them to be localized using field gradients, analogous to nuclear spins in MRI (Figure 1). These addressable transmitters operated as magnetic spins (ATOMS) can then be coupled to biological sensing and actuation circuits, enabling a wide variety of biomedical applications. To facilitate rapid translation, ATOMS have been designed to operate within frequency and power ranges of MRI and make use of widely available MRI components for spatial encoding and communication.

ATOMS Chip Architecture

The system architecture of our ATOMS chip consists of a magnetic sensor, a two-stage chopper amplifier, an analog-to-digital converter (ADC), a phase-locked loop (PLL), a power amplifier (PA), an on-chip coil, and a control logic with digital signal processing (DSP) [Figure 2(a)]. A base frequency of 500 MHz (f_0) was chosen based on compatibility with available equipment.

The basic operation of our proof-of-concept device consists of three phases: magnetic phase, excitation phase, and transmission phase [Figure 2(b)]. During the magnetic phase, ATOMS devices sense, process, and store the applied magnetic field at each of their locations. The excitation phase starts when the radio-frequency (RF) pulse is applied. The frequency of the RF pulse f_0 is acquired, and the on-chip PLL locks to this frequency. The transmission phase follows, during which each device radiates a signal with a shifted frequency proportional to the measured magnetic field. The on-chip coil is used to acquire the excitation RF signal and emit the response of the chip. By measuring the shifted frequencies, the location of each device can then be determined by mapping them back into space.

Magnetic Sensing and Signal Conditioning

The schematic of the magnetic sensing and signal conditioning unit is shown in Figure 3. The magnetic sensor is an on-chip split-drain magnetic field-sensitive field-effect transistor (MagFET) that measures the applied magnetic field orthogonal to the chip (B_Z). This Hall-effect device generates a differential current ΔI proportional to B_Z and the bias current I_{MS}, according to $\Delta I = \mu_H B_Z (L/W) I_{MS} G_H$, where μ_H is the Hall mobility, W and L are the dimensions of the MagFET, and G_H is a geometry factor. The sensitivity of the device is then defined as $S_I = \Delta I / I_{MS} B_Z$. We optimized the size of the device to maximize ΔI given our power budget and low voltage supply, resulting in an aspect ratio W/L of 0.71.

The MagFET's output is amplified by a transimpedance amplifier (TIA) and a low-noise amplifier (LNA). To minimize noise at low frequencies, a chopper amplifier is formed by adding chopper modulators in the TIA and the LNA. The TIA consists of a current buffer (current amplifier, IAMP) and a pair of matched resistors that converts the current into voltage. The current buffer is a low-voltage cascode current mirror that provides low-input impedance with good matching. Having a current gain greater than one implies higher TIA gain but also higher power

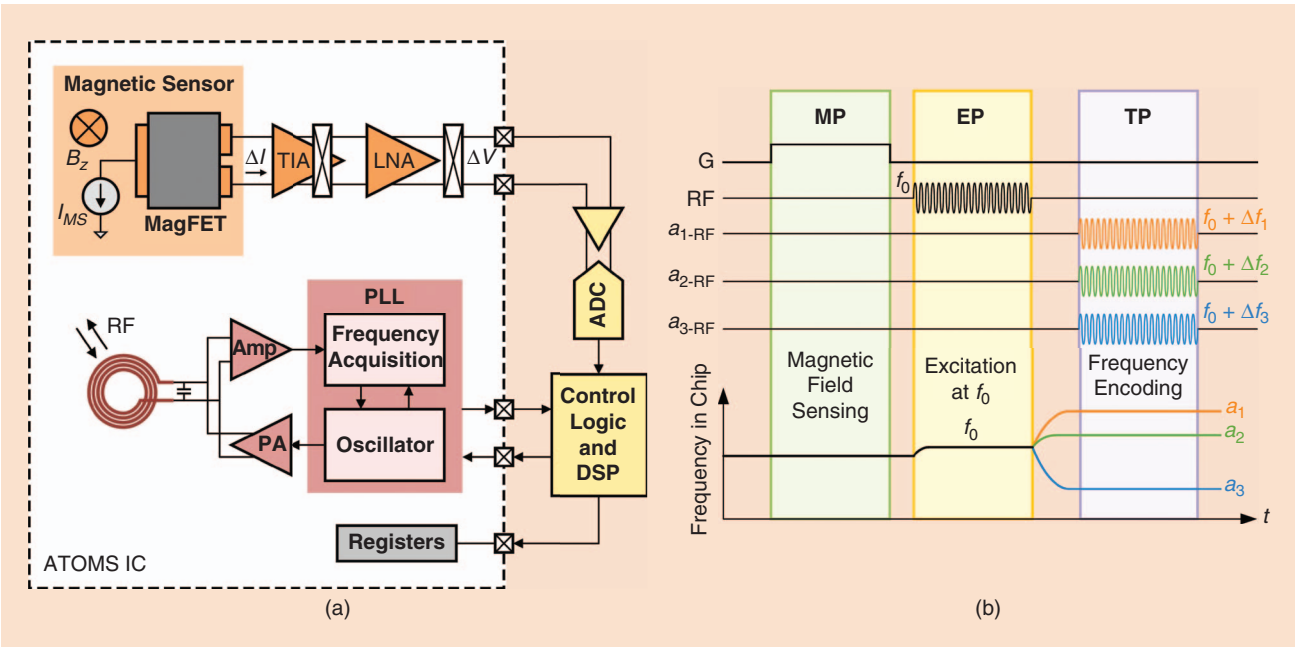

FIGURE 2: (a) A system architecture and (b) basic operation principle of an ATOMS device. MP: magnetic phase; EP: excitation phase; TP: transmission phase. (Figure taken from [6].)

consumption and higher process variation. Given that we have other gain stages and a limited power budget, we chose a gain of one in this design. The LNA is a capacitive-feedback amplifier with pseudoresistors that uses a fully differential folded cascode at its core. This topology provides high gain and good noise performance at low voltage supplies. The output of the amplifier is then digitized for processing (e.g., averaging) and storage.

The amplifier is calibrated using six dual-current digital-to-analog converters (DACs) that reduce the offset in the MagFET, TIA, and LNA. Each dual DAC is composed of a pair of 4-b DACs that are used instead of a single higher-resolution DAC to reduce area. Due to the low supply, an additional set of current mirrors is used to inject the calibrating currents. Our current implementation calibrates the amplifier manually, but it can be easily integrated in a future version following a successive-approximation-register-like binary search algorithm to achieve a self-calibrating stage.

Frequency Acquisition, Encoding, and Transmission

ATOMS devices need to detect the presence of the RF excitation pulse, keep its oscillation frequency f_0 after the RF excitation is removed, and shift f_0 during transmission based on the previously measured local magnetic field. The proposed PLL shown in Figure 4 was designed to address these requirements.

An oscillator detector is added to the PLL to sense the presence of the RF pulse and to enable control of the PLL loop. This block generates a control signal (*osc*) that indicates the presence of the RF pulse and a sampling signal (*sa*) to be used for sampling of V_{ctrl}. During the excitation phase, the chip closes this loop for frequency acquisition and synchronization, and the PLL locks the internal oscillator to the RF pulse. The oscillation frequency of the voltage-controlled oscillator (VCO) f_{osc} is then measured by sampling V_{ctrl} using a switch capacitor network. Because the PLL needs to keep f_{osc} without a reference, we use a low K_{VCO} to minimize the sensitivity to variations in V_{ctrl}. A digital calibration corrects for process variations and brings the oscillation frequency of the VCO within the PLL locking range.

When the RF excitation pulse ends, the oscillation detector senses this transition, and the transmission phase starts. During this phase, the chip opens the PLL loop, shifts the frequency of the VCO proportional to the measured magnetic field, and feeds the oscillator's output to the PA for transmission. In this phase, the VCO becomes a free-running oscillator with a central frequency determined by the sampled voltage V_{sa}. To generate frequency shifts, we use a current DAC with 6-b resolution. The global controller keeps the PLL in this mode during a fixed time window (e.g., 1 ms) before changing phases to wait for the next pulse. It is important to note that the phase noise of the VCO during transmission plays an important role in determining the localization resolution.

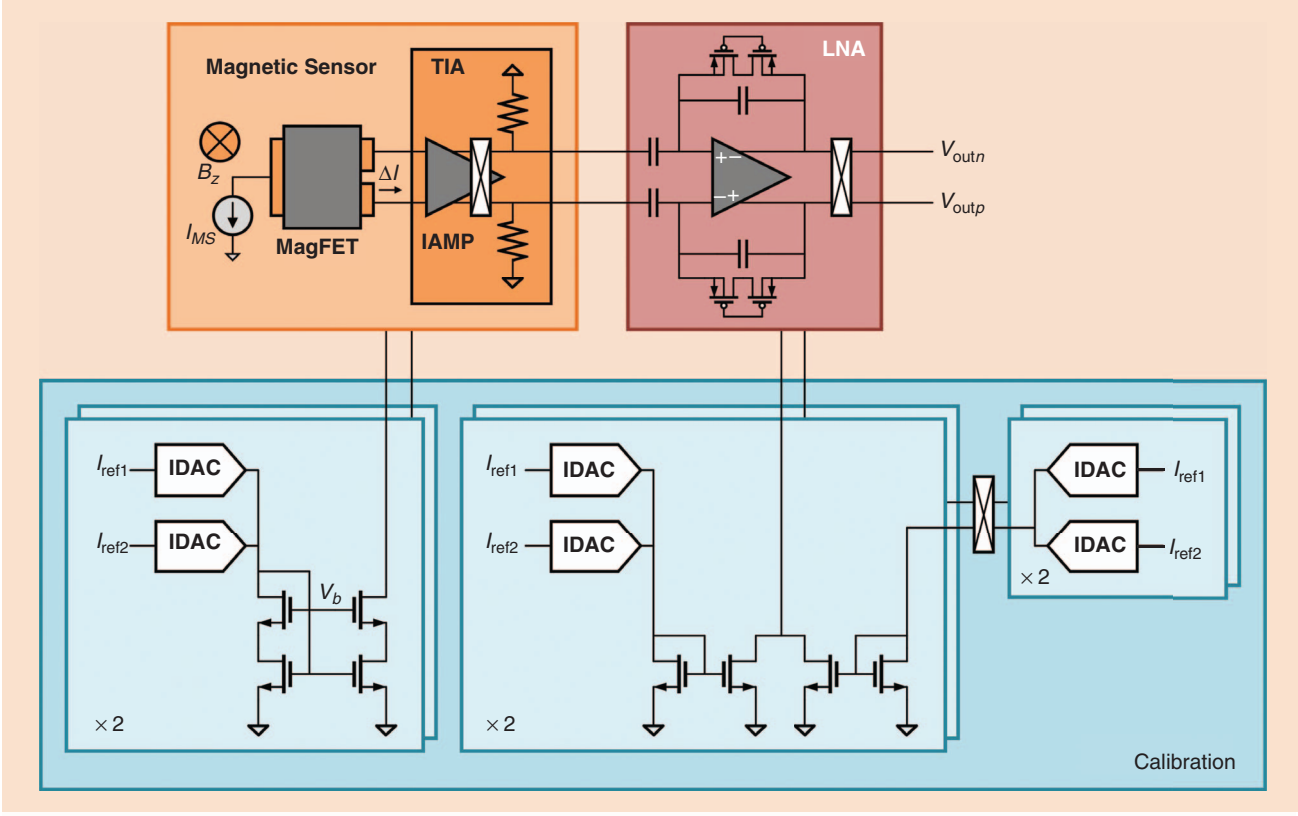

FIGURE 3: A schematic of the magnetic-sensing and signal-conditioning unit. IDAC: Current (I) digital-to-analog converter.

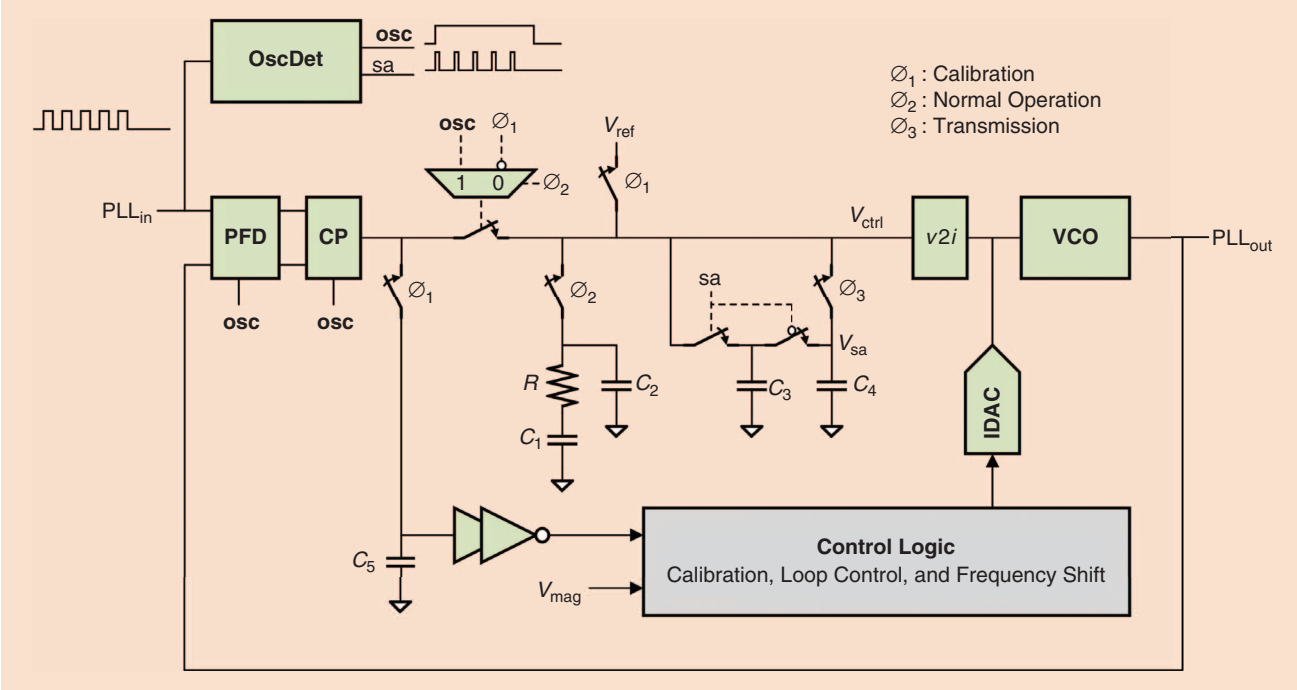

FIGURE 4: A schematic of the PLL. v2i: voltage-to-current. CP: charge pump; PFD: phase-frequency detector; OscDet: oscillation detector.

We use a differential current-controlled ring oscillator and a voltage-to-current stage as the VCO. The ring oscillator uses current-starved inverters as the delay elements. We choose a ring oscillator instead of an LC oscillator because of its small area and lower power consumption. Although ring oscillators have higher phase noise compared to LC oscillators, the phase noise requirements can be relaxed by adjusting the bandwidth of the external receiver.

Measurement Results

In this work, we focused on integrating the critical components of the system in a single chip: the magnetic sensor, amplifiers, PLL, PA, and the on-chip coil for frequency locking and radiation. The ADC and control logic have more relaxed requirements due to the low processing speed (up to a few kilohertz) and can be integrated into the system in future versions with minimal impact on size and power requirements. The chip was fabricated in a standard 180-nm, 1.8-V complementary metal–oxide–semiconductor process, operates at 1.2 V, and occupies an area of 1.8 mm × 1.2 mm (Figure 5). Importantly, the area occupied by the core elements is only 0.61 mm^2.

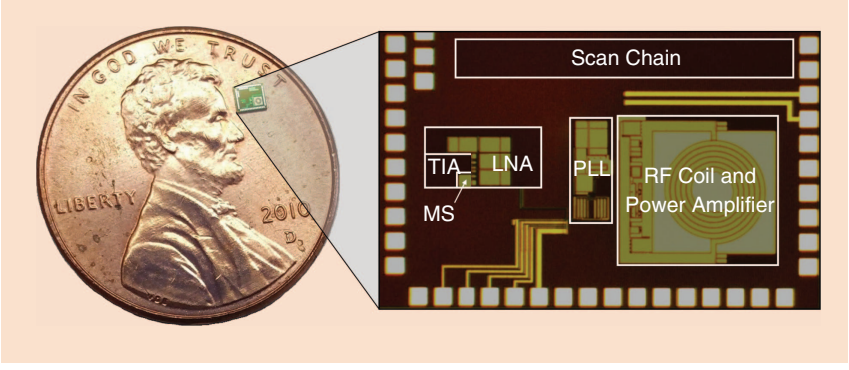

FIGURE 5: An ATOMS microchip compared with a U.S. penny and die micrograph. The chip has a size of 1.8 mm × 1.2 mm. MS: magnetic sensor. (Images taken from [6].)

The on-chip MagFET has a size of 20 μm × 28 μm, a measured sensitivity of 3.29%/T, and a measured total input referred noise of 625.48 μT between 2 Hz and 100 kHz. The TIA and LNA have a gain of 317.38 kΩ and 25 dB, respectively. The overall bandwidth of the amplifier is 1 kHz, and the chopper frequency is set to 763 Hz. These results translate to a sensitivity of 5.48 V/T at the output of the LNA. The on-chip coil has a size of 420 μm × 420 μm and a quality factor of 4.6 at 500 MHz. The PLL has an integrated root-mean-square jitter (10 kHz–10 MHz) of 60 ps when it is locked and 308 ps when it is unlocked. The minimum frequency shift is set to 1.4 MHz for a total range of 88.5 MHz centered at f_0. The power consumption of the chip is dominated by the magnetic sensor, the internal oscillator, and the radiation elements, and it is measured to be 339 μW on average. Whereas in this design, power is provided externally, such low power consumption allows wireless power delivery in future versions. An external ADC with 12-b resolution and sample rate of 763 Hz is used for all our measurements. The control logic and DSP are implemented

in an external field-programmable gate array (FPGA). The controller runs at 1 MHz to transmit 150 b via a serial interface, and the DSP runs at 763 Hz.

Characterization of ATOMS Chip

We characterized the performance of the ATOMS chip using the test setup shown in Figure 6(a). The excitation RF pulse was produced using a signal generator, and the response of the chip was captured by a receive coil, amplified by an LNA, and analyzed using a spectrum analyzer and a real-time oscilloscope. A second signal generator was used for pulse modulation and synchronization between transmitter and receiver channels. We only used the wired output of the chip to measure and evaluate the response of the system during the excitation phase in initial electrical characterization. All other measurements were taken from the wireless signal picked up by the external receiver coil. We used a permanent magnet to generate the magnetic field gradient, which was mapped using a gaussmeter.

The ATOMS chip first measured the local magnetic field and used a moving-average filter of 128 samples at 763 Hz (implemented in the FPGA) to reduce noise. The internal oscillator, during this phase, oscillated at its natural frequency. When the excitation RF pulse (400 μs pulsewidth) was applied, the chip wirelessly detected its presence, locked the internal oscillator to this signal, and measured its frequency. When the RF pulse was removed, the chip sensed this transition and shifted its oscillation frequency for transmission [Figure 6(b)]. Note that the latency in communication between the chip and the external control logic (FPGA) caused a delay of ~35 μs in frequency encoding due to the use of a serial interface for data transfer. During this time, the PLL was opened and the oscillation frequency briefly returned to its initial value. For this experiment, the output of the chip was measured for 800 μs at 31 different values of the magnetic field.

The spectral profile of the chip at 13 magnetic field strengths is shown

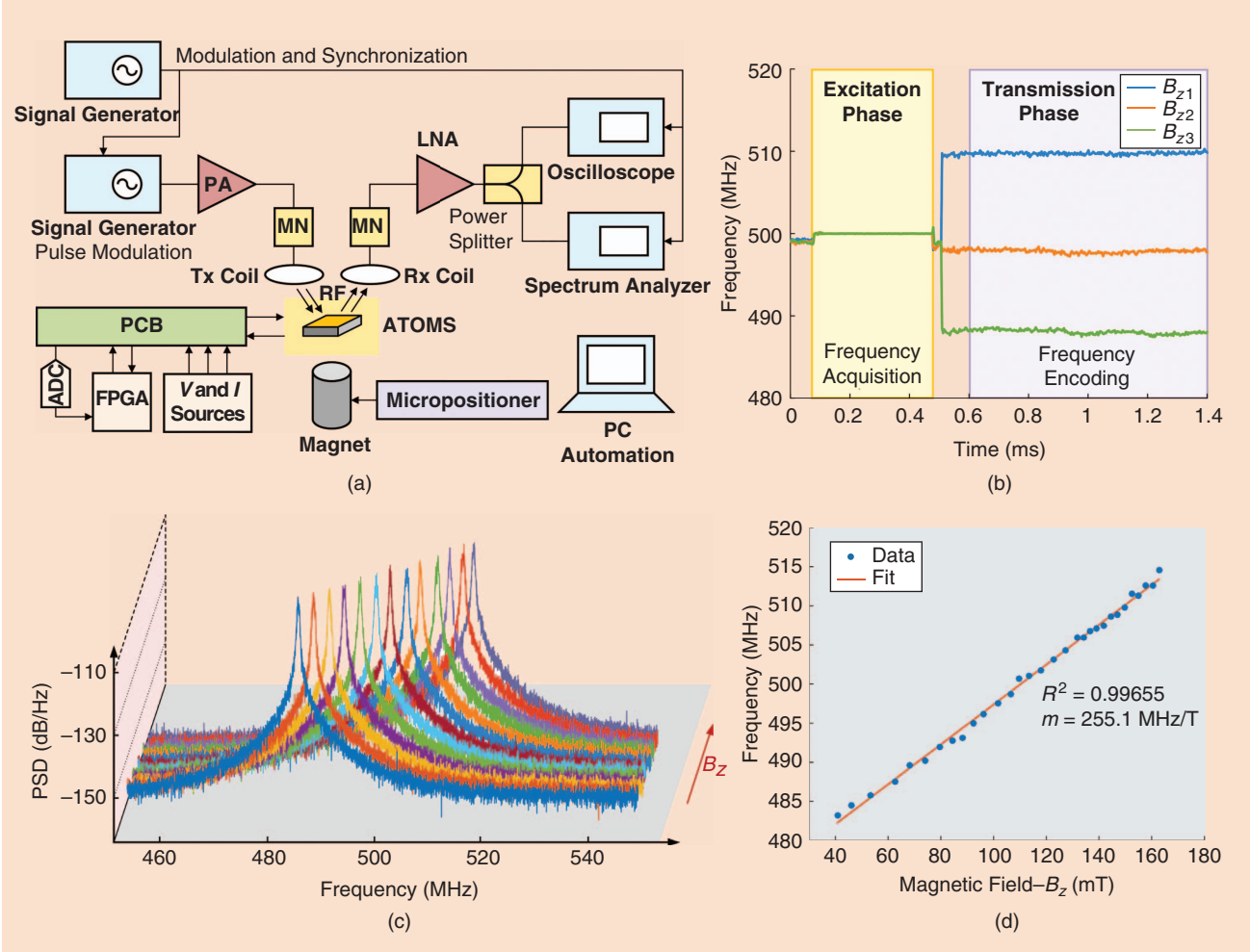

FIGURE 6: (a) An illustration of the test setup for ATOMS characterization. The ATOMS chip was exposed to 31 different values of the magnetic field. (b) Frequency response during excitation phase and transmission phase, showing frequency acquisition and frequency encoding for three magnetic field magnitudes. (c) A spectral profile of the ATOMS chip at 13 magnetic field strengths. The arrow indicates an increase in the magnetic field B_z. (d) The oscillation frequency of the chip as a function of the magnetic field and its linear regression. PCB: printed circuit board; RX: receiver; TX: transmitter; V & I: voltage and current; MN: matching network. (Figure taken from [6].)

in Figure 6(c). As expected, the oscillation frequency of the chip changed proportional to the field strength. It showed a full-width at half-maximum or 3-dB bandwidth of 600 kHz. For each field strength, the oscillation frequency was estimated by calculating the center frequency of the peak of the power spectral density (PSD). A linear relationship between oscillation frequency and magnetic field was then found in the range of

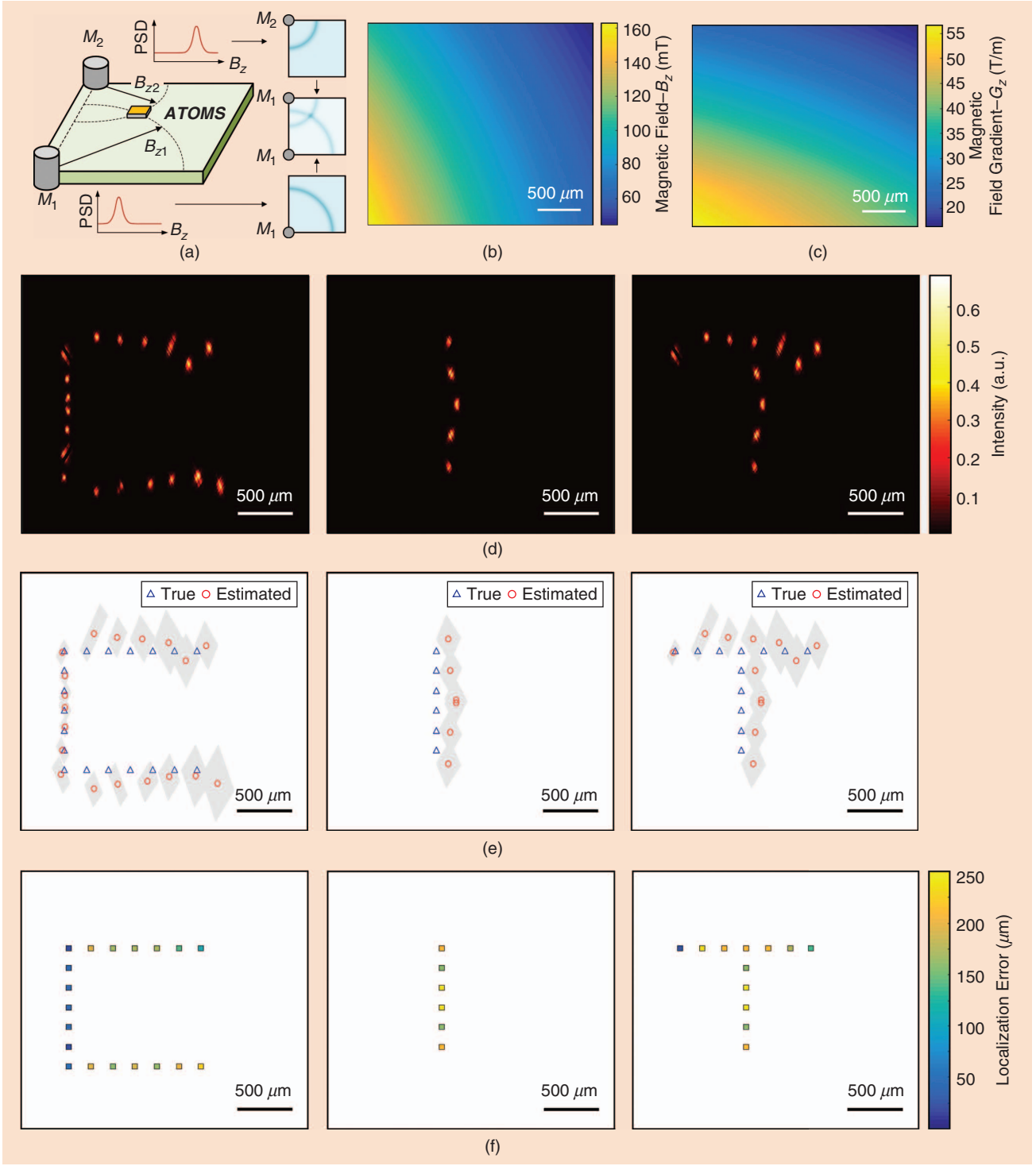

FIGURE 7: (a) An illustration of the 2-D localization experiment, in which two magnets were used to generate two magnetic field gradients in different directions. The ATOMS chip was moved relative to the position of both magnets. (b) 2-D mapping of the magnetic field and (c) the magnetic field gradient generated by the magnets. The magnets were placed at locations (0, 0) mm for M_1 and (0, 2.6) mm for M_2. Only M_1 is shown because both magnets are of the same kind. (d) Localization results of three different experiments where the ATOMS chip was placed at positions to form the letters C, I, T. (e) The estimated and true position of each experiment. The shaded region indicates the standard deviation. (f) The localization errors of each experiment. Each square in the figure shows the error of its corresponding position in space. N = 32 for (e). (Figure taken from [6].)

480–520 MHz and 40–170 mT [Figure 6(d)]. We defined a parameter to represent this relationship, calling it its *gyromagnetic ratio*, γ_{ATOMS}, by analogy to nuclear spins. The ATOMS chip has a measured γ_{ATOMS} of 255.1 MHz/T. The location of the chip in a magnetic field profile $B_Z = g(x)$ can then be obtained according to

$$\hat{x} = g^{-1}\left(\frac{\Delta f + \Delta f_0}{\gamma_{ATOMS}}\right),$$

where g^{-1} is the inverse function of B_Z, Δf is the frequency shift generated by the chip, and Δf_0 is the frequency shift offset.

Two-Dimensional Localization

We performed a two-dimensional (2-D) localization experiment using the test setup shown in Figure 7(a). We used two permanent magnets (M_1 and M_2) to apply magnetic field gradients in two different directions [Figure 7(b) and (c)]. Adding and removing one magnet at a time allowed us to apply a sequence of two field gradients, analogous to the design of pulse sequences in MRI. The frequency response of the chip in each gradient defined a curve of possible positions corresponding to a specific magnetic field magnitude [B_{Z_1} and B_{Z_2} in Figure 7(a)]. We defined the functions $P_{M_1}(x, y)$ and $P_{M_2}(x, y)$ as the mapping of the PSD of the chip's response into the 2-D magnetic field space of M_1 and M_2, respectively. We then obtained the 2-D position from the center of the peak of $P_{M_{12}}(x, y) = (P_{M_1}/P_{M_1,\max})(P_{M_2}/P_{M_2,\max})$, representing the point of intersection.

We used this system to track the location of an ATOMS chip while translating it in space to write the letters C, I, and T. As expected, the three letters can be clearly identified [Figure 7(d)]. The estimated and true positions of the ATOMS chip at each measurement point are shown in Figure 7(e). A localization error of lower than 250 μm was measured for all cases [Figure 7(f)], and the error depended on the magnitude of the magnetic field gradient, with lower errors where the gradient is highest.

In Vivo Localization

We localized our ATOMS device following subcutaneous implantation in the shoulder area of an anesthetized mouse according to approved Institutional Animal Care and Use Committee procedures [Figure 8(a)]. A permanent magnet placed above the mouse generated the magnetic field profile, and a transmit/receive coil was used for RF excitation and signal reception. In preparation for this experiment, the chip was placed in the shaft of a small printed circuit board and encapsulated using a silicon elastomer. We moved the chip to four different locations on

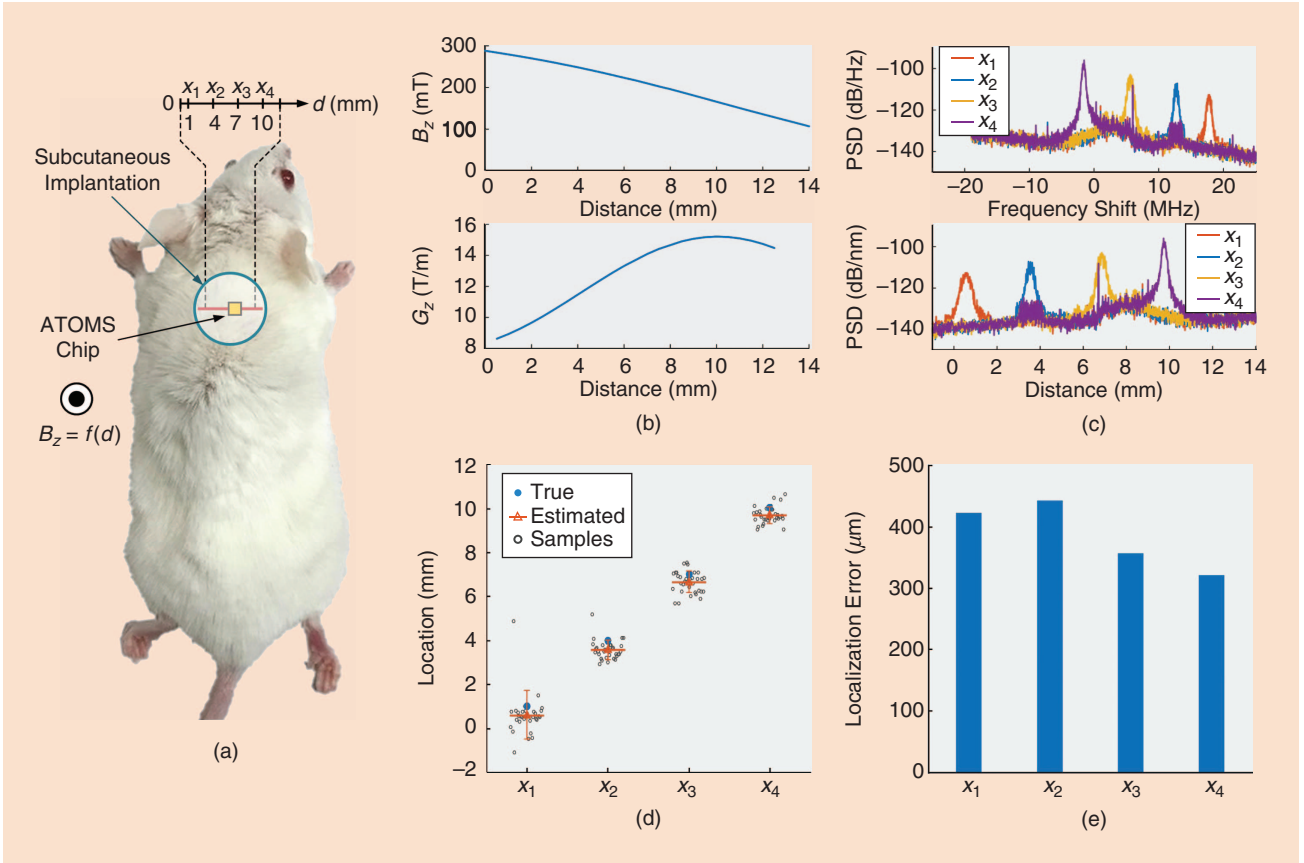

FIGURE 8: (a) An illustration of the in vivo localization experiment. (b) The magnetic field and magnetic field gradient produced by the magnet. (c) Frequency shift-location mapping. The figure shows the PSD of the received signal as a function of frequency shift (top) and distance (bottom). (d) The estimated and true positions of all four cases. Gray circles represent all data points. (e) The localization error of the experiment. $N = 32$ for *(d)* Error bars represent ± standard deviation. (Figure taken from [6].)

This technology is expected to have substantial scientific and clinical impact.

a single axis using a micropositioner. A stronger magnet was used to increase the effective field of view to more than 12 mm by generating the magnetic field profile shown in Figure 8(b). Due to this new profile, the chip was tuned to accommodate the new magnetic field range by calibrating the magnetic sensor offset and reducing the overall gain of the system. In this case, γ_{ATOMS} was measured to be 170.7 MHz/T. The PSD of the received signals exhibited four different peaks corresponding to the target locations [Figure 8(c)]. A localization error of lower than 500 μm was measured for all cases [Figure 8(d) and (e)], and this error exhibited less positional dependence than previous experiments, in agreement with the more linear magnetic field. This experiment demonstrates that ATOMS-enabled devices can be localized in living biological tissues.

Conclusions

The ATOMS technology—microscale devices that mimic the behavior of nuclear spins to enable their spatial localization using the principles of magnetic resonance—provides an elegant solution to the problem of locating and interfacing with microscale in vivo biosensors by decoupling the dependence of RF methods from body composition and time-sensitive parameters (e.g., time of arrival or received-signal strength). As a result, this technology combines the benefits of frequency encoding using magnetic field gradients and highly sensitive RF receivers. Because ATOMS technology does not require a superconductive magnet, it offers a more affordable and simpler alternative compared to actual MRI methods that image nuclear spin precession.

As a result, this technology is expected to have substantial scientific and clinical impact. On the scientific front, many problems in biology require the study of physiological processes in their in vivo context. By developing ATOMS-powered biosensors and actuators and distributing them to appropriate organs, such as the brain, vasculature, the gastrointestinal tract, and the lymphatic system, biologists will be able to carry out new studies of disease-relevant processes in living animals. On the clinical front, there is major interest in advancing small pill technologies from single, centimeter-sized wireless cameras to distributed micron-sized devices capable of migrating through the vasculature (or other orifices) and performing local imaging, sensing, and interventions, thus reducing the need for invasive diagnostic and surgical procedures.

References

[1] G. Ciuti, A. Menciassi, and P. Dario, "Capsule endoscopy: From current achievements to open challenges," *IEEE Rev. Biomed. Eng.*, vol. 4, pp. 59–72, Oct. 2011.

[2] A. P. Alivisatos, A. M. Andrews, E. S. Boyden, M. Chun, G. M. Church, K. Deisseroth, J. P. Donoghue, S. E. Fraser, J. Lippincott-Schwartz, L. L. Looger, S. Masmanidis, P. L. McEuen, A. V. Nurmikko, H. Park, D. S. Peterka, C. Reid, M. L. Roukes, A. Scherer, M. Schnitzer, T. J. Sejnowski, K. L. Shepard, D. Tsao, G. Turrigiano, P. S. Weiss, C. Xu, R. Yuste, and X. Zhuang, "Nanotools for neuroscience and brain activity mapping," *ACS Nano*, vol. 7, no. 3, pp. 1850–1866, 2013.

[3] B. J. Williams, S. V. Anand, J. Rajagopalan, and M. T. A. Saif. (2014, Jan.). A self-propelled biohybrid swimmer at low Reynolds number. *Nat. Commun.* [Online]. 5. Available: https://www.nature.com/articles/ncomms4081

[4] B. J. Nelson, I. K. Kaliakatsos, and J. J. Abbott, "Microrobots for minimally invasive medicine," *Annu. Rev. Biomed. Eng.*, vol. 12, pp. 55–85, Aug. 2010.

[5] T. D. Than, G. Alici, H. Zhou, and W. Li, "A review of localization systems for robotic endoscopic capsules," *IEEE Trans. Biomed. Eng.*, vol. 59, no. 9, pp. 2387–2399, 2012.

[6] M. Monge, A. Lee-Gosselin, M. Shapiro, and A. Emami, "Localization of microscale devices in vivo using addressable transmitters operated as magnetic spins," *Nat. Biomed. Eng.*, vol. 1, no. 9, pp. 736–744, 2017.

About the Authors

Azita Emami (azita@caltech.edu) received her B.S. degree from Sharif University of Technology, Tehran, Iran, in 1996 and her M.S. and Ph.D. degrees in electrical engineering from Stanford University, California, in 1999 and 2004, respectively. She is the Andrew and Peggy Cherng Professor of Electrical Engineering and Medical Engineering at California Institute of Technology (Caltech), Pasadena, and a Heritage Medical Research Institute investigator. She also serves as the executive officer (department head) for electrical engineering. From 2004 to 2006, she was with IBM T.J. Watson Research Center before joining Caltech in 2007. Her current research interests include integrated circuits and systems, integrated photonics, optical interconnects, wearable and implantable devices for neural recording, neural stimulation, sensing, and drug delivery. She is currently an associate editor for *IEEE Journal of Solid-State Circuits* and an IEEE Solid-State Circuits Society Distinguished Lecturer.

Manuel Monge (manuel.monge@usc.edu) received his B.S. degree (with honors) in electrical engineering from the Pontifical Catholic University of Peru, Lima, in 2008 and his M.S. and Ph.D. degrees in electrical engineering from the California Institute of Technology (Caltech), Pasadena, in 2010 and 2017, respectively. He is currently an assistant professor of electrical engineering at the University of Southern California (USC), Los Angeles. He spent a year working at Neuralink Corp., developing ultrahigh-bandwidth brain–machine interfaces, before joining USC in 2018. His research interests focus on the miniaturization of medical electronics by combining and integrating physical and biological principles into the design of microscale integrated circuits. He is the recipient of the 2017 Charles Wilts Prize from the Department of Electrical Engineering at Caltech for outstanding independent research in electrical engineering leading to a Ph.D. and the 2017 Demetriades-Tsafka-Kokkalis Prize in Biotechnology from the Division of Engineering and Applied Science at Caltech for the best thesis in the field of biotechnology. He is a Member of the IEEE.

SSC